



OPEN

Superconductivity in anti-post-perovskite vanadium compounds

Bosen Wang & Kenya Ohgushi

Institute for Solid State Physics, University of Tokyo, Kashiwanoha, Kashiwa, Chiba 277-8581, Japan.

Superconductivity, which is a quantum state induced by spontaneous gauge symmetry breaking, frequently emerges in low-dimensional materials. Hence, low dimensionality has long been considered as necessary to achieve high superconducting transition temperatures (T_C). The recently discovered post-perovskite (ppv) MgSiO_3 , which constitutes the Earth's lowermost mantle (D'' layer), has attracted significant research interest due to its importance in geoscience. The ppv structure has a peculiar two-dimensional character and is expected to be a good platform for superconductivity. However, hereunto, no superconductivity has been observed in isostructural materials, despite extensive investigation. Here, we report the discovery of superconductivity with a maximum T_C of 5.6 K in V_3PnN_x ($\text{Pn} = \text{P}, \text{As}$) phases with the anti-ppv structure, where the anion and cation positions are reversed with respect to the ppv structure. This discovery stimulates further explorations of new superconducting materials with ppv and anti-ppv structures.

Since the discovery of high- T_C superconductivity in cuprates with the layered-perovskite (pv) structure¹, extensive effort has been devoted to finding other superconducting materials. After a quarter century of investigation, many layered superconducting families have been discovered, such as a ruthenate Sr_2RuO_4 ², boride MgB_2 ³, hafnium nitride chloride⁴, cobaltate $\text{Na}_x\text{CoO}_2 \cdot y\text{H}_2\text{O}$ ⁵, an intercalated graphite C_6Ca ⁶, a chalcogenide Cu_xTiSe_2 ⁷, and iron-based pnictides and chalcogenides^{8,9}. The layered characteristics of the host crystal structures are widely believed to be essential in producing superconductivity due to the anisotropic electronic structures. This provides an important reference for the design of superconducting materials and the exploration of new mechanisms for superconductivity^{1,2,4-6}. Recently, the ppv transition of MgSiO_3 was discovered using a laser-heated diamond anvil cell^{10,11}. Consequently, this phase has received more attention because it is considered to be the main constitute of the Earth's lowermost mantle (D'' layer, *ca.* 2700–2900 km deep) (Fig. 1a). The ppv crystal structure is comprised of alternately-stacked SiO_6 octahedra and Mg atoms along the *b* axis and it has typical two-dimensional characteristics. This has motivated research into the physical phenomena of this phase, including superconductivity. However, ppv- MgSiO_3 is stable only under extreme conditions (120 GPa and 2200 °C)¹² and is unquenchable to ambient pressure, which has restricted further research into chemical substitution and carrier doping of the structure. Therefore, there have been attempts to establish analogue materials that are stable under ambient conditions. Almost 20 ppv-type compounds have been identified to date, including the MgGeO_3 , NaIrO_3 , and CaBO_3 ($B = \text{Ru}, \text{Rh}, \text{Sn}, \text{Ir}, \text{and Pt}$) oxides, $\text{Na}(\text{Mg}, \text{Zn})\text{F}_3$ fluorides and $(\text{U}, \text{Th})\text{MnSe}_3$ chalcogenides¹³⁻¹⁹. As with perovskite-type materials, many interesting physical phenomena have been observed in ppv-type materials, such as metal-insulator phase transition¹³ and low-dimensional magnetism¹⁷. However, no superconductivity has been reported so far for the ppv family, because most compounds with ppv structure are Mott insulators owing to the strong electron correlation effect.

In this letter, we report the observation of superconductivity in V_3PnN_x ($\text{Pn} = \text{P}, \text{As}$). These compounds crystallize in the filled Re_3B structure with the orthorhombic Cmcm (#63) space group, as depicted in Fig. 1b²⁰. The positions occupied by the anions and cations are opposite to those of the ppv structure. Considering also the nomenclature of the anti-pv structure^{21,22}, we call this structure the anti-ppv structure (see crystal structure details in Section I of the Supplementary Information). The anti-ppv-type V_3PnN_x is composed of alternately-stacked NV_6 octahedral layers and PnV_8 bicapped trigonal prisms layers along the *b* axis, which gives rise to quasi-two-dimensional electronic states. Within the *ac*-plane, NV_6 octahedra are connected by edge sharing along the *a* axis and corner sharing along the *c* axis²⁰. Here, we also notice that V-V metallic bonds play the key role in stabilizing this structure²⁰.

Results

Figure 2a presents the electrical resistivity (ρ) of V_3PnN_x ($\text{Pn} = \text{P}, \text{As}$) as a function of temperature (T). The room temperature resistivities $\rho_{300\text{K}}$ are approximately 340 and 240 $\mu\Omega \text{ cm}$ for V_3PN and V_3AsN , respectively. ρ

SUBJECT AREAS:

SUPERCONDUCTING
PROPERTIES AND
MATERIALS

METALS AND ALLOYS

ELECTRONIC PROPERTIES AND
MATERIALS

STRUCTURAL GEOLOGY

Received
5 June 2013Accepted
12 November 2013Published
29 November 2013

Correspondence and requests for materials should be addressed to B.W. (bswang@issp.u-tokyo.ac.jp) or K.O. (ohgushi@issp.u-tokyo.ac.jp)

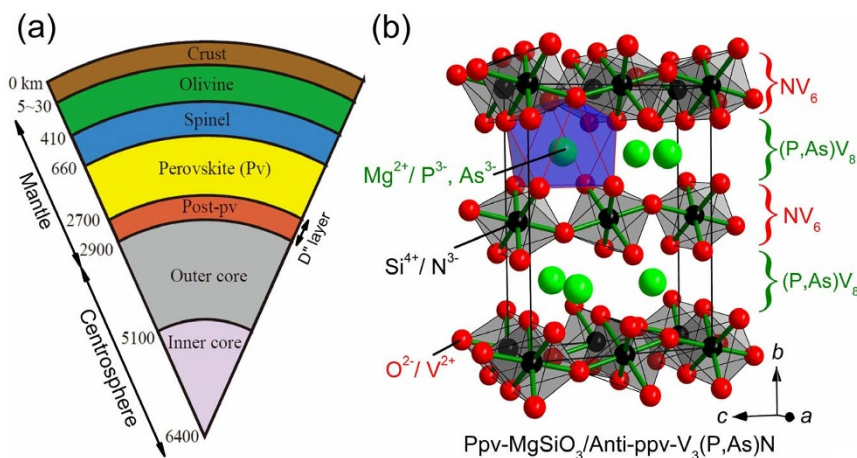


Figure 1 | Schematic illustration of Earth's interior and crystal structures of ppv-MgSiO₃/anti-ppv-V₃PnN. (a) The outermost solid shell is the crust composed of a variety of rocks. The mantle below the crust has layer structures corresponding to the structural transition induced by pressure in Mg-Si-O system. The lowermost layer is called the D'' layer, where the main constitute is the ppv-type silicate. The outer and inner cores below the mantle consist of liquid and solid iron alloys, respectively. (b) Crystal structure of ppv-MgSiO₃ and anti-ppv-V₃PnN ($Pn = P, As$) with the Cmcm (#63) space group. Solid lines represent a unit cell. The anti-ppv structure has layer structures composed of NV₆ octahedra and PnV₈ polyhedra.

decreases gradually with cooling (metallic behaviour) and drops sharply to zero at $T_C = 4.2$ and 2.6 K for V₃PN and V₃AsN (Fig. 2c), respectively, which indicates the appearance of superconductivity. The width of the transition temperature is narrow (*ca.* 0.3 K), which implies good sample quality. Figure 2d presents the magnetic susceptibility (M/H) under zero-field cooling (ZFC) and field cooling (FC) conditions at $H = 10$ Oe. The superconducting volume fraction estimated from ZFC data at 1.8 K are approximately 190 and 167% for V₃PN and V₃AsN, respectively. The volume fractions exceeding 100% is attributable to the polycrystalline nature of samples. The specific heat shown in Fig. 2e has a sudden increase around T_C . These results provide unambiguous evidence for the bulk superconductivity in V₃PnN ($Pn = P, As$).

Detailed measurements of the field-dependent resistivity and magnetization presented in Figs. 3a–f allow for better characterization of the superconducting state. The H -dependence of ρ (Figs. 3a–c) gives the upper critical field H_{C2} , as shown in Fig. 3g. There is another weak

transition above H_{C2} that originates from a small amount of the VN_x impurity phase, as shown in Fig. S1(a). Close to T_C , H_{C2} is linearly dependent on T in accordance with the Werthamer-Helfand-Hohenberg theory²³. Using the formula $H_{C2}(0) = -0.693T_C dH_{C2}/dT$ provided H_{C2} at the ground state; $H_{C2}(0) = 34.9$ and 27.9 kOe was obtained for V₃PN and V₃AsN, respectively. According to the Bardeen-Copper-Schrieffer (BCS) theory²⁴, the H_{C2} value is related to the coherent length ξ , as $H_{C2} = \Phi_0/2\pi\xi^2$ (where Φ_0 is the magnetic flux quantum). Using this formula, $\xi = 9.7$ and 10.9 nm are obtained for V₃PN and V₃AsN, respectively. The magnetization isotherms at 1.8 K exhibit typical type-II superconductor behaviour (insets of Figs. 3d, 3f). The lower critical field H_{C1} was determined from the magnetic field, where the magnetization departs from the linear H -dependence (indicated by arrows in Figs. 3d, 3f). The temperature dependence of H_{C1} is well fitted with the empirical function $H_{C1}(T) = H_{C1}(0)[1 - \alpha(T/T_C)^2]$ (where α is the fitting parameter), and the lower critical fields obtained at the ground state are $H_{C1}(0) = 207$ and

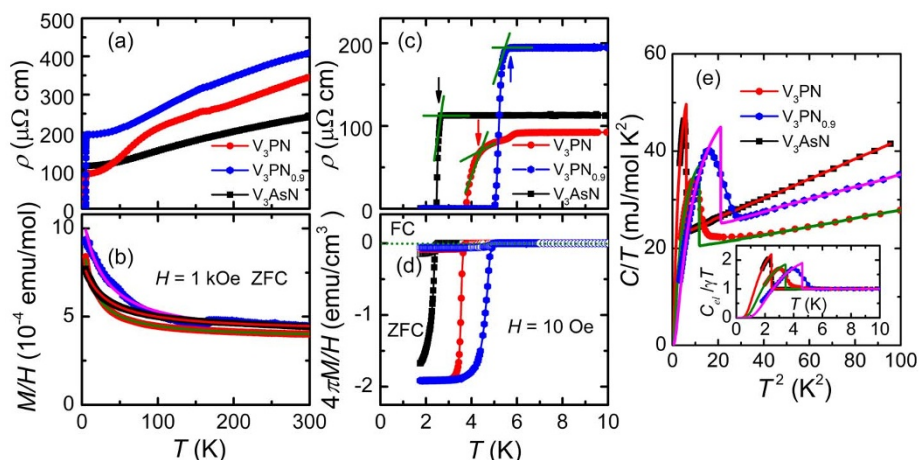


Figure 2 | Evidence for bulk superconductivity in V₃PnN ($Pn = P, As$). (a) Temperature (T) dependent resistivity (ρ) at zero magnetic field (H). (b) DC susceptibility (M/H) curve under the ZFC condition at $H = 1$ kOe. Solid lines indicate fitting results (see text). (c) Enlargement of low-temperature resistivity data. Arrows indicate the superconducting transition temperature (T_C). (d) Low-temperature M/H - T curve under ZFC and FC conditions at $H = 10$ Oe. (e) Temperature dependence of specific heat (C/T) at zero magnetic field. Solid lines indicate fitting with $C = \gamma T + \beta T^3$ in the normal state and the function based on the BCS model in the superconducting state. Inset shows the $C_{el}/\gamma T_C$ value, where C_{el} is the electron contribution of the specific heat. The solid curve is calculated from the BCS model with an isotropic gap.

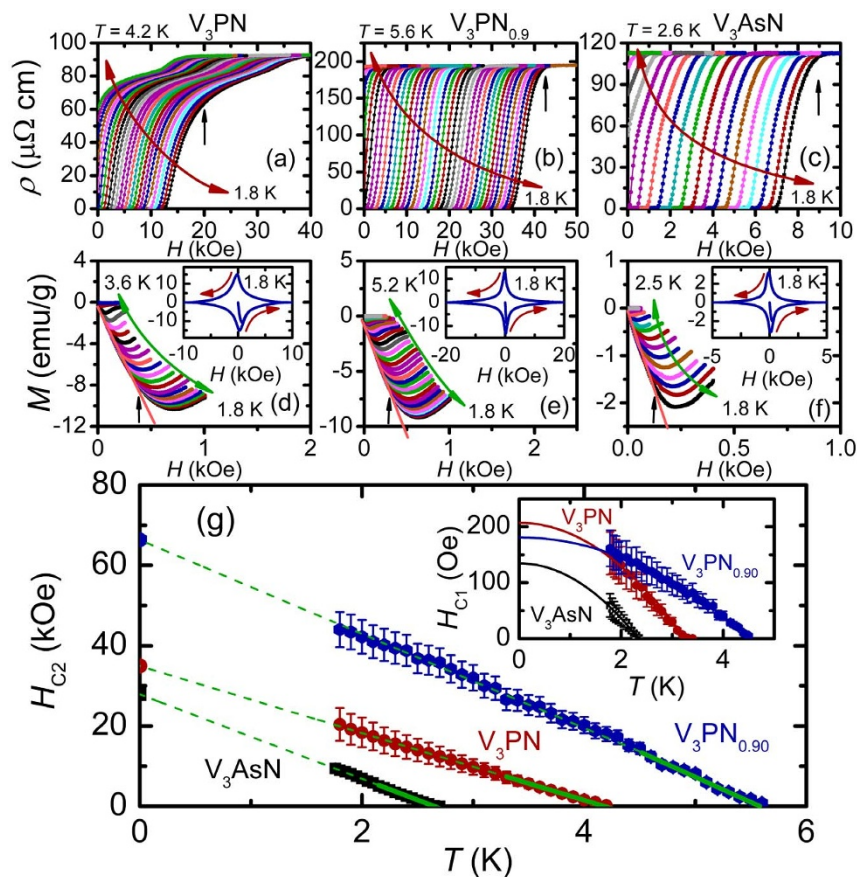


Figure 3 | Characterization of the superconductivity in V_3PnN ($Pn = P, As$). Magnetic field (H) dependence of (a–c) resistivity (ρ) and (d–f) magnetization (M) at fixed temperatures. Arrows in (a–c) indicate the upper critical field (H_{C2}) at 1.8 K. There is another weak transition above H_{C2} that originates from a small amount of the VN_x impurity phase, as shown in Fig. S1(a). Arrows in Figs. (d–f) indicate the lower critical field (H_{C1}), where M departs from the linear H -dependence. Insets in (d–f) are magnetization isotherms at 1.8 K over a wider H range. (g) Temperature (T) dependence of the upper and lower critical fields (H_{C2} and H_{C1}). Solid lines indicate fitting results (see text).

134 Oe for V_3PN and V_3AsN , respectively (inset of Fig. 3g). The London penetration depths λ_L , and the Ginzburg-Landau parameters κ are estimated from the formula $H_{C2}/H_{C1} = 2\kappa^2/\ln\kappa$ with $\kappa = \lambda_L/\xi$ to be $\lambda_L = 157$ and 187 nm and $\kappa = 16.2$ and 17.2 for V_3PN and V_3AsN , respectively.

The appearance of superconductivity in both $Pn = P$ and As compounds, as well as N-deficient systems (Fig. 4), indicate that the V -3d electrons are predominantly responsible for the emergence of superconductivity. The specific heat was closely examined to reveal bosons that act as the glue for Cooper pairs. The specific heat at the normal state can be well fitted using the function $C = \gamma T + \beta T^3$ (Fig. 2e), where the former and latter terms represent the electron and phonon contributions, respectively. We estimated $\gamma = 19.5$ and 22.0 mJ/mol K², and $\beta = 0.083$ and 0.20 mJ/mol K⁴ for V_3PN and V_3AsN , respectively. The $\Delta C/\gamma T_C$ value (inset of Fig. 2e), where ΔC is the specific heat jump at T_C , is approximately 0.86 and 1.22 for V_3PN and V_3AsN , respectively. These values are slightly smaller than 1.43 expected for a typical BCS superconductor with a weak-coupling limit, which implies that the electron-phonon coupling is the glue for the Cooper pairs^{24,25}. The Debye temperature was estimated to be $\theta_D = 489$ and 364 K for V_3PN and V_3AsN , respectively, using the relationship $\beta = 12\pi^4 NR/5\theta_D^3$ (where N is the number of atoms in a formula unit, 5, and R is the gas constant). It is worth noting that θ_D for V_3PN is larger than that for V_3AsN , because materials with smaller mass exhibit harder phonons. From the McMillan formula, $T_C = (\theta_D/1.45) \exp\{-1.04(1 + \lambda_{ph})/[\lambda_{ph} - \mu^*(1 + 0.62\lambda_{ph})]\}$ ²⁶, together with the assumption of the Coulomb pseudopotential $\mu^* = 0.15$, the electron-phonon coupling constants

can be estimated as $\lambda_{ph} = 0.55$ and 0.54 for V_3PN and V_3AsN , respectively. These are typical values for phonon-mediated weakly coupling BCS superconductors^{24,25,27}.

On the other hand, the importance of a strong electron correlation effect manifests itself from an analysis of the Wilson ratio $R_w = \pi^2 k_B^2 \chi_s / 3\mu_B^2 \gamma$, where k_B is the Boltzmann constant, χ_s is the spin susceptibility, and μ_B is the Bohr magneton²⁸. The magnetic susceptibility ($\chi = M/H$) in the normal state exhibits weakly T -dependent behaviour and can be well fitted to the formula $\chi = \chi_0 + C_{CW}/(T - \theta)$ (Fig. 2b), where χ_0 is a temperature-independent term, C_{CW} is the Curie-Weiss constant, and θ is the Weiss temperature. The fitting results give $\chi_0 = 4.13 \times 10^{-4}$ and 3.75×10^{-4} emu/mol, $C_{CW} = 1.09 \times 10^{-2}$ and 8.08×10^{-3} emu K/mol, and $\theta = -26.5$ and -13.0 K for V_3PN and V_3AsN , respectively. Using the obtained χ_0 values as χ_s , we acquire $R_w = 1.42$ and 1.45 for V_3PN and V_3AsN , respectively. The enhancement from the Fermi liquid value of 1 indicates a moderate electron correlation effect in the present compounds. Moreover, the ρ values in the normal state are in the order of 10^{-4} Ω cm (Figs. 2a, 2c), which is much larger than typical ρ values for conventional intermetallic compounds and indicates strong electron-electron interaction. Therefore, magnetic fluctuations originating from the strong electron correlation effect could not be excluded as the pairing glue for Cooper pairs.

Besides elucidation of the microscopic mechanism, identification of the chemical factors responsible for the appearance of superconductivity is important to further increase T_C in this new family of superconductors. Therefore, we have focused on the effects of N-defects on the superconductivity. The T_C values determined from

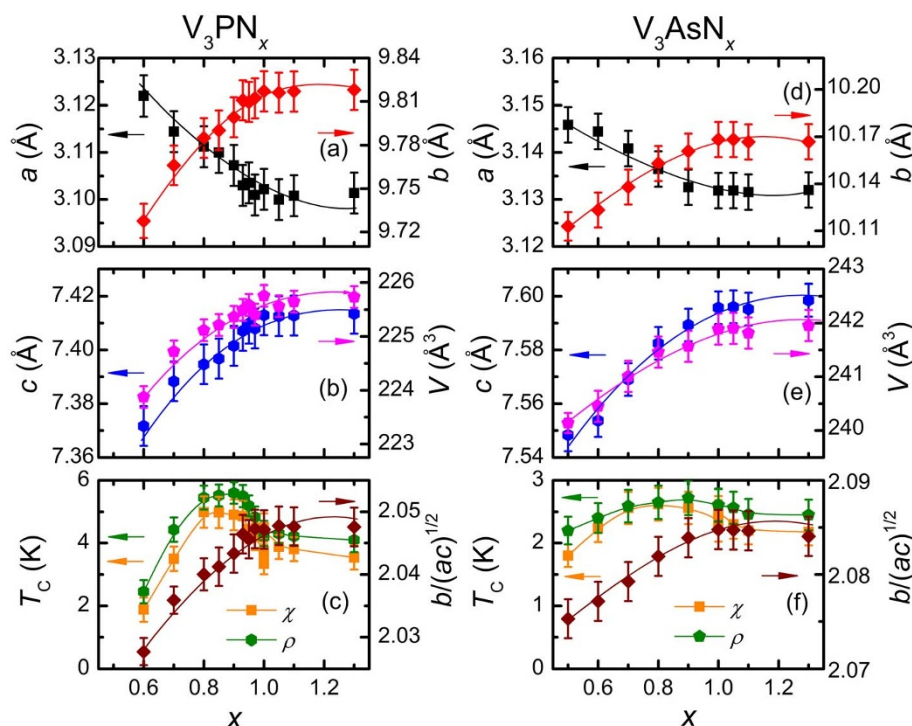


Figure 4 | Lattice parameters and superconducting transition temperature as a function of N-content (x). The values of a , b , c , V and T_C were determined from resistivity (ρ) and susceptibility (χ) data for (a–c) V_3PN_x and (d–f) V_3AsN_x . The $b/[ac]^{1/2}$ values, which quantify the two dimensionality of the systems, are also plotted in (c) and (f).

the low-temperature resistivity and magnetization of V_3PN_x ($x = 0.6$ – 1.3) and V_3AsN_x ($x = 0.5$ – 1.3) (x is the nominal composition, and the actual composition is expected to be less than 1) have been summarized in Figs. 4c and 4f (raw data are shown in Fig. S3 of supplementary information). For both cases, T_C is significantly enhanced with increasing x in the low x region, then decreases slightly after reaching a maximum at just below the stoichiometric composition ($x = 1$). The highest T_C achieved was 5.6 K for $V_3PN_{0.9}$, and the corresponding electronic properties are presented in Figs. 2a–e, 3b, 3e, and 3g. In addition, as x increases, the lattice expands along the b and c axes, and contracts along the a axis, which results in a slight increase of the unit cell volume. Here, we note that the $b/(ac)^{1/2}$ value, which quantifies the two-dimensionality of the system, is well correlated with the T_C values, as shown in Figs. 4c and 4f.

Discussion

On the basis of these experimental results, we now discuss the mechanism of superconductivity in V_3PnN . The strong correlation between T_C and $b/(ac)^{1/2}$ values suggests that the quasi two dimensionality of crystal structure plays an important role in the appearance of superconductivity. This suggestion is reinforced by the higher T_C for V_3PN than for V_3AsN . The former system has stronger in-plane coupling because the smaller atomic radius of P compared with that of As makes the in-plane V–V bond distances shorter, resulting in the enhanced hybridization of $3d$ orbitals in the plane; moreover, more ionic character of V–P bonds compared with V–As bonds due to the larger electronegativity of P than that of As also enhances the two-dimensionality of the system. Then, how this two dimensionality favor the superconductivity? If the electron-phonon interaction mediates Cooper pairs as suggested by electronic properties, the T_C value is considered to be enhanced by the larger density of states at the Fermi energy in low dimensional systems. Another possibility is that the electron correlation effect pronounced in the low dimensional crystal structure due to the smaller kinetic energy of electrons

stabilizes the superconducting states. Generally, T_C is known to be very sensitive to various factors in reported superconductors. Therefore, further detailed studies are required to identify the mechanism of superconductivity, especially on hybridization of the V- $3d$ and N- $2p$ bands, the direct-overlapping of V- $3d$ orbitals across two V atoms, and the change in carrier density introduced by N-defects.

To summarize, we have discovered superconductivity with maximum T_C at 5.6 and 2.6 K for V_3PN_x and V_3AsN_x with the anti ppv structure. Two-dimensionality is the key for the appearance of superconductivity; however, to elucidate the microscopic mechanism of superconductivity, further experimental and theoretical studies are required. These findings should stimulate future experimental and theoretical research on ppv-type materials to explore advanced functionalities.

Methods

An optimized synthesis method²⁰ was employed. Powders of elemental vanadium (99.999%), vanadium nitride (99.9%), and phosphorus (99.99%) or arsenic (99.9%) were mixed in a stoichiometric ratio, pressed into pellets in a nitrogen-filled glove box, and then sealed in a quartz tube under 0.3 atm of argon gas. The quartz tube was slowly heated to 673 K, held for 24 h to avoid rapid volatilization of the phosphorus or arsenic, then heated to 1273 K for 12 h and held for 120 h. After quenching the tubes to room temperature, the product was pulverized and pressed into pellets. The pellets were annealed inside a quartz tube at 1273 K for 48 h. To remove oxide impurities during this procedure, the V_3PN_x and V_3AsN_x pellets were wrapped with molybdenum and tantalum foil, respectively, inside the quartz tube. The as-synthesized samples were dark grey coloured with a metallic luster and were stable in air. The samples were characterized using powder X-ray diffraction (Rigaku, Smartlab) with Cu K α radiation.

The detailed structural parameters were obtained by Rietveld refinement using Rietica software²⁹. Details of the analysis are presented in section I of the Supplementary Information. Magnetic, electrical, and heat capacity measurements were performed using a commercial apparatus (Quantum Design) from 1.8 to 300 K. DC resistivity measurements were performed using the four-probe method with gold paste as electrodes.

1. Bednorz, J. G. & Müller, K. A. Possible high T_C superconductivity in the Ba-La-Cu-O system. *Z. Phys. B* **64**, 189–193 (1986).



2. Maeno, Y. *et al.* Superconductivity in a layered perovskite without copper. *Nature* **372**, 532–534 (1994).
3. Nagamatsu, J. *et al.* Superconductivity at 39 K in magnesium diboride. *Nature* **410**, 63–64 (2001).
4. Yamanaka, S. *et al.* Superconductivity at 25.5 K in electron-doped layered hafnium nitride. *Nature* **392**, 580–582 (2001).
5. Takada, K. *et al.* Superconductivity in two-dimensional CoO₂ layers. *Nature* **422**, 53–55 (2003).
6. Thomas, E. W. *et al.* Superconductivity in the intercalated graphite compounds C₆Yb and C₆Ca. *Nature Phys.* **1**, 39–41 (2005).
7. Morosan, E. *et al.* Superconductivity in Cu_xTiSe₂. *Nature Phys.* **2**, 544–550 (2006).
8. Kamihara, Y. *et al.* Iron-based layered superconductor La[O_{1-x}F_x]FeAs ($x = 0.05-0.12$) with $T_C = 26$ K. *J. Am. Chem. Soc.* **130**, 3296–3297 (2008).
9. Chen, X. H. *et al.* Superconductivity at 43 K in SmFeAsO_{1-x}F_x. *Nature* **435**, 761–762 (2008).
10. Murakami, M. *et al.* Post-perovskite phase transition in MgSiO₃. *Science* **304**, 855–858 (2004).
11. Oganov, A. R. & Ono, S. Theoretical and experimental evidence for a post-perovskite phase of MgSiO₃ in earth's D'' layer. *Nature* **430**, 445–448 (2004).
12. Belonoshko, A. B. *et al.* High-pressure melting of MgSiO₃. *Phys. Rev. Lett.* **94**, 195701 (2005).
13. Ohgushi, K. *et al.* Metal-insulator transition in Ca_{1-x}Na_xIrO₃ with post-perovskite structure. *Phys. Rev. B.* **74**, 241104(R) (2006).
14. Yamaura, K. *et al.* Synthesis and magnetic and charge-transport properties of the correlated 4d post-perovskite CaRhO₃. *J. Am. Chem. Soc.* **131**, 2722–2726 (2009).
15. Cheng, J.-G. *et al.* Stress-induced perovskite to post-perovskite in CaIrO₃ at room temperature. *Phys. Rev. B.* **82**, 132103 (2010).
16. Bremholm, M. *et al.* NaIrO₃-A pentavalent post-perovskite. *J. Solid State Chem.* **184**, 601–607 (2011).
17. Shirako, Y. *et al.* Integer spin-chain antiferromagnetism of the 4d-oxide CaRuO₃ with post-perovskite structure. *Phys. Rev. B.* **83**, 174411 (2011).
18. Yakovlev, S. *et al.* High-pressure structural behavior and equation of state of NaZnF₃. *J. Solid State Chem.* **182**, 1545–1549 (2009).
19. Ijjaali, I. *et al.* Syntheses and characterization of the actinide manganese selenides ThMnSe₃ and UMnSe₃. *J. Solid State Chem.* **177**, 257–261 (2004).
20. Boller, H. & Nowotny, H. Komplexcarbide und-nitride mitaufgefülltem Re₃B-type. *Monatsh. Chem.* **99**, 721–725 (1968).
21. He, T. *et al.* Superconductivity in the non-oxide perovskite MgCNi₃. *Nature* **411**, 54–56 (2001).
22. Takayama, T. *et al.* Strong coupling superconductivity at 8.4 K in an antiperovskite phosphide SrPt₃P. *Phys. Rev. Lett.* **108**, 237001 (2012).
23. Werthamer, N. R. *et al.* Temperature and purity dependence of the superconducting critical field, H_{C2} . III. Electron spin and spin-orbit effects. *Phys. Rev.* **147**, 295–302 (1966).
24. Bardeen, J., Cooper, L. N. & Schrieffer, J. R. Theory of superconductivity. *Phys. Rev.* **108**, 1175–1204 (1957).
25. Kresin, V. Z. On the critical temperature for any strength of the electron-phonon coupling. *Phys. Lett. A* **122**, 434–438 (1987).
26. McMillan, W. L. Transition temperature of strong-coupled superconductors. *Phys. Rev.* **167**, 331–344 (1968).
27. Kresin, V. Z. & Parchomenko, V. Thermodynamic properties of strong-coupling superconductors. *Sov. Phys. Solid State* **16**, 2180–2184 (1975).
28. Wilson, K. The renormalization group: Critical phenomena and the Kondo problem. *Rev. Mod. Phys.* **47**, 773–840 (1975).
29. Rietveld, H. M. A profile refinement method for nuclear and magnetic structures. *J. Appl. Cryst.* **2**, 65–71 (1969).

Acknowledgments

The authors acknowledge discussions with Prof. Y. Ueda, Dr. Y. Hirata, Dr. Y. Q. Zhang, and Dr. F. Du. We also thank M. Isobe and T. Yamauchi for their technical supports. This work was supported by the Grant Program of the Sumitomo Foundation, and the Grant Program of the Murata Science Foundation.

Author contributions

B.W. prepared the samples and carried out the experiments. The authors equally contributed to analysing the results. B.W. wrote the paper with assistance from K.O. K.O. directed the research.

Additional information

Supplementary information accompanies this paper at <http://www.nature.com/scientificreports>

Competing financial interests: The authors declare no competing financial interests.

How to cite this article: Wang, B. & Ohgushi, K. Superconductivity in anti-post-perovskite vanadium compounds. *Sci. Rep.* **3**, 3381; DOI:10.1038/srep03381 (2013).



This work is licensed under a Creative Commons Attribution-NonCommercial-NoDerivs 3.0 Unported license. To view a copy of this license, visit <http://creativecommons.org/licenses/by-nc-nd/3.0>